

Layered Perovskite Doping with Eu^{3+} and β -diketonate Eu^{3+} Complex

Daniele Cortecchia,* Wojciech Mróz, Giulia Folpini, Tetiana Borzda, Luca Leoncino, Ada Lili Alvarado-Leaños, Emily Mae Speller, and Annamaria Petrozza*



Cite This: *Chem. Mater.* 2021, 33, 2289–2297



Read Online

ACCESS |



Metrics & More

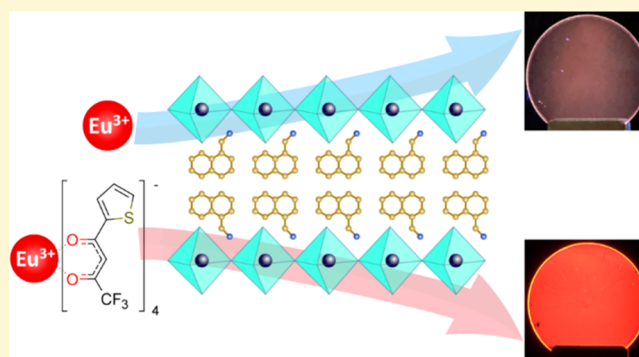


Article Recommendations



Supporting Information

ABSTRACT: Metal halide perovskites are attracting great interest for the fabrication of light-emitting devices encompassing light-emitting diodes, lasers, and scintillators. As the field develops, perovskite doping emerges as a promising way to enrich the material functionalities and enhance the luminescence yield and tunability. While Mn^{2+} addition has been well explored, doping with lanthanides has received less attention, even though their intense and line-like luminescence is interesting for a wide range of applications. In this work, we study the doping of $\text{NMA}_2\text{PbBr}_4$ layered perovskites with Eu^{3+} and Eu^{3+} tetrakis β -diketonate complex. By exploiting the antenna effect of the naphthalene-based functional cation ($\text{NMA} = 1\text{-naphthylmethylammonium}$), direct sensitization of Eu^{3+} is obtained; nevertheless, it is not very efficient due to the non-optimal energy level alignment with the resonance acceptor level of the lanthanide. Protection of Eu^{3+} in the form of tetrakis β -diketonate complex grants a more ideal coordination geometry and energetic landscape for the energy transfer to europium in the perovskite matrix, allowing for a nearly 30-fold improvement in luminescence yield. This work sets the basis for new synthetic strategies for the design of functional perovskite/lanthanide host–guest systems with improved luminescence properties.



INTRODUCTION

Metal halide perovskites (MHPs) are attracting great interest for a wide range of light-emitting applications including light-emitting diodes (LEDs) and transistors,^{1,2} lasers and scintillators.^{3,4} The surge in device performance strongly motivates the investigation of synthetic strategies to further enrich the properties of MHPs and provide them with new functionalities.⁵ Considering the three-dimensional (3D) MHP structure with general formula ABX_3 , B-site doping with d-block and f-block elements has been pursued to boost the luminescence properties. CsPbCl_3 nanocrystals has been the most investigated host, although in a few cases successful doping have been reported also in layered perovskites.^{5–9} Among the notable examples, energy transfer to Mn^{2+} leads to broadband orange luminescence with quantum yield up to 30–40% and has been employed for LEDs and luminescent solar concentrators.^{8,10,11} Within lanthanides, Yb^{3+} , $\text{Yb}^{3+}/\text{Er}^{3+}$, and $\text{Yb}^{3+}/\text{Ce}^{3+}$ have been the most studied systems since they allow efficient NIR luminescence with extraordinary photoluminescence quantum yields (PLQYs) surpassing 100% aided by a quantum cutting process.^{12–15} Doping with other rare-earth metals, despite a few promising attempts,^{8,14} has not been thoroughly investigated. Among these, trivalent europium (Eu^{3+}) has a characteristic intense red luminescence which makes it very interesting for light-emitting devices with high color purity,^{16,17} optical

amplifiers and lasers,^{18,19} sensors and spectroscopic probes.²⁰ Since the closed $5s^2$ and $5p^6$ shells efficiently screen the partially filled 4f shell, where the transitions responsible for the luminescence occur, the electronic configuration is only weakly perturbed thus resulting in extremely narrow emission lines and long excited state lifetimes.^{21,22} Eu^{3+} doping has been shown in combination with a wide range of host matrices like glasses, xerogels, polysilsesquioxanes, metal organic frameworks, polyoxometalates, organic polymers as well as in intercalation compounds with layered materials, such as layered double hydroxides and clays.²³ Concerning MHPs, europium has been used to improve the operational and phase stability of perovskite solar cells^{24,25} and employed to expand the luminescence properties of CsPbCl_3 and CsPbBr_3 nanocrystals for application in LEDs.^{14,26–30} However, europium doping in low-dimensional MHPs and the use of functional organic cations to improve the lanthanide sensitization within the perovskite framework have been scarcely investigated.

Received: October 20, 2020

Revised: February 24, 2021

Published: March 21, 2021



Compared to 3D perovskites, layered perovskites offer greater synthetic and structural flexibility which are beneficial to carefully explore the photophysical and structural design required to achieve efficient luminescence through Eu^{3+} doping.³¹ In lanthanides, intraconfigurational electric dipole (ED) $f-f$ transitions are strictly spin and parity forbidden. Selection rules are partially relaxed by spin-orbit coupling and crystal-field perturbations which induce mixing of the levels of the 4f configuration with orbitals having opposite-parity wavefunctions, such as 5d orbitals.^{21,22,32} Even though these mechanisms allow ED transitions to occur, Eu^{3+} (likewise other lanthanide ions) suffers from very low absorption coefficients, in turn resulting in weak luminescence. This issue is typically solved by (1) including Eu^{3+} in a strongly asymmetric site of the host matrix³³ and (2) sensitizing Eu^{3+} with organic ligands, where their larger absorption coefficient is exploited to more efficiently absorb light and transfer energy to the lanthanide (antenna effect),³⁴ with the energy transfer process typically involving a nonradiative transition from the triplet state of the organic ligand to an excited state of Eu^{3+} .²¹ To populate a resonance level of Eu^{3+} , there should be an overlap between the ligand phosphorescence and the absorption of the lanthanide, and the triplet of the ligand should be positioned at an energy above a resonance level of Eu^{3+} .²⁰ Second, the lanthanide ion should be protected from non-radiative deactivation of excited states through vibration of the lattice or ligands.²¹ An in-depth understanding of the transfer mechanisms in Eu^{3+} excitation is a crucial step for the achievement of high luminescence efficiencies.

Here, we study two-dimensional (2D) perovskites doping by means of Eu^{3+} ions and a europium chelate. We show that functional organic molecules can be exploited to provide effective sensitization of the lanthanide ion embedded in the perovskite matrix. Naphthalene-based derivatives, such as naphthoyltrifluoroacetone and naphthalene-functionalized cyclen, have been used in the past as antennae to populate the Eu^{3+} excited state.^{35–37} In this case, we directly employ NMA = 1-naphthylmethylammonium as a templating cation to form the perovskite host NMA_2PbX_4 (where X = Br, Cl) and discuss its role in the sensitization of Eu^{3+} by means of temperature and power-dependent measurements and time-resolved photoluminescence (TRPL) spectroscopy. Although lanthanide luminescence is observed with direct B-site doping, better population of Eu^{3+} excited states is achieved by protection of Eu^{3+} in the form of tetrakis β -diketonate complex,¹⁷ which leads to the formation of an intercalation compound in the layered structure of the perovskite with nearly 30-fold improvement in luminescence quantum yield. This work expands the range of synthetic tools for the development of functional perovskites with improved luminescence properties, with great relevance for applications in light-emitting and photonic devices.

RESULTS AND DISCUSSION

$\text{NMA}_2\text{PbBr}_4$ (Figure 1a) films were synthesized by spin-coating of dimethylformamide (DMF) solutions of stoichiometric amounts of the precursors (NMA)Br and PbBr_2 .

Two doping strategies were pursued: (1) substitutional doping with Eu^{3+} ions to form $\text{NMA}_2\text{PbBr}_4:\text{Eu}$ was achieved by addition of EuCl_3 to the perovskite spin-coating solution; (2) doping with europium chelate was obtained by initially synthesizing the tetrakis β -diketonate complex $\text{Eu}(\text{tta})_4\text{P}(\text{Ph})_4$ [hereinafter $\text{Eu}(\text{L})$; Figure 1b], where Eu^{3+} is coordinated by the four ligands tta = thenoyltrifluoroacetone, thus resulting in an

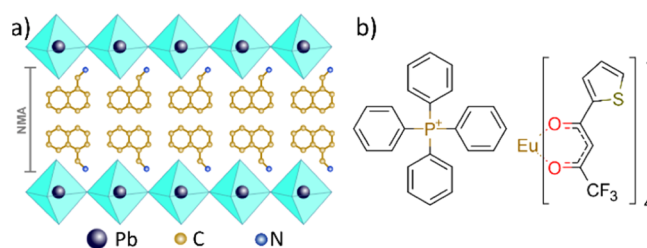


Figure 1. (a) Schematic representation of $\text{NMA}_2\text{PbBr}_4$ and (b) europium complex $\text{Eu}(\text{tta})_4\text{P}(\text{Ph})_4$.

anionic complex, with the electric neutrality maintained by the tetraphenylphosphonium $\text{P}(\text{Ph})_4^+$ counter ion. Note that the ligand choice has been also driven by the following key requirements: (1) compatibility with the perovskite processing conditions, including good thermal stability to sustain the annealing process; (2) compatibility with the ionic perovskite host; and (3) spectral match with the perovskite's luminescence (a necessary condition to realize energy transfer from the perovskite to the complex). $\text{Eu}(\text{tta})_4\text{P}(\text{Ph})_4$ satisfies all these conditions. The ionic nature of the tetrakis complex favors its retention in the perovskite ionic lattice by coulombic interaction. The preformed complex is added to the spin-coating solution to form the doped system $\text{NMA}_2\text{PbBr}_4:\text{Eu}(\text{L})$. In both cases, doping was performed by adding a 10% mol content of Eu^{3+} with respect to Pb^{2+} .

Figure 2a shows the X-ray diffraction (XRD) patterns of the obtained thin films. Due to the strong preferential orientation typical of 2D perovskites, only three diffraction peaks (4.7, 9.38, and 14.1°) are observed for $\text{NMA}_2\text{PbBr}_4$. The retention of the same diffraction pattern in $\text{NMA}_2\text{PbBr}_4:\text{Eu}$ and $\text{NMA}_2\text{PbBr}_4:\text{Eu}(\text{L})$ indicates that the perovskite is formed also in the presence of the dopants. The weaker diffraction of $\text{NMA}_2\text{PbBr}_4:\text{Eu}(\text{L})$ suggests a reduction in crystallinity, as can be expected by the introduction of the bulky complex. In both cases, we also observe a small but clear shift of the diffraction peaks to smaller angles (inset in Figure 2a), indicating the increase in interplanar distance. While this trend can be explained by partial incorporation of chlorine in $\text{NMA}_2\text{PbBr}_4:\text{Eu}$ due to the addition of EuCl_3 (see Figure S1), lattice expansion is particularly interesting for $\text{NMA}_2\text{PbBr}_4:\text{Eu}(\text{L})$, where it points to the formation of an intercalation compound similar to other perovskites incorporating organic luminophores.³⁸ From XRD, we estimate an interplanar distance between the adjacent inorganic layers of 18.8 Å in $\text{NMA}_2\text{PbBr}_4$, which is comparable to that reported for $(2\text{-NMA})_2\text{PbBr}_4$, where 2-NMA = 2-naphthylmethylammonium.³⁹ Considering a diameter of about 11 Å for $[\text{Eu}(\text{tta})_4]^-$,⁴⁰ it is possible for the europium complex to intercalate within the perovskite layers by inducing disorder of the organic cations as well as local widening of the interplanar distance. Absorption spectra (Figure 2b) further support this assumption. In all of the three compounds, only minimal differences are found in the excitonic absorption peak around 385 nm, indicating that the inorganic framework is largely preserved. On the contrary, a big reduction in absorbance is found for $\text{NMA}_2\text{PbBr}_4:\text{Eu}(\text{L})$ below 275 nm, a region dominated by the $\pi-\pi^*$ transitions of the organic cation NMA (Figure S2), which can be attributed to a strong disruption of the NMA stacking pattern and modifications in the intermolecular forces holding the crystal upon insertion of $\text{Eu}(\text{L})$, which are likely to affect the nature of the collective excitations of the resulting solid.^{41–43} Incorporation of $\text{Eu}(\text{L})$ is

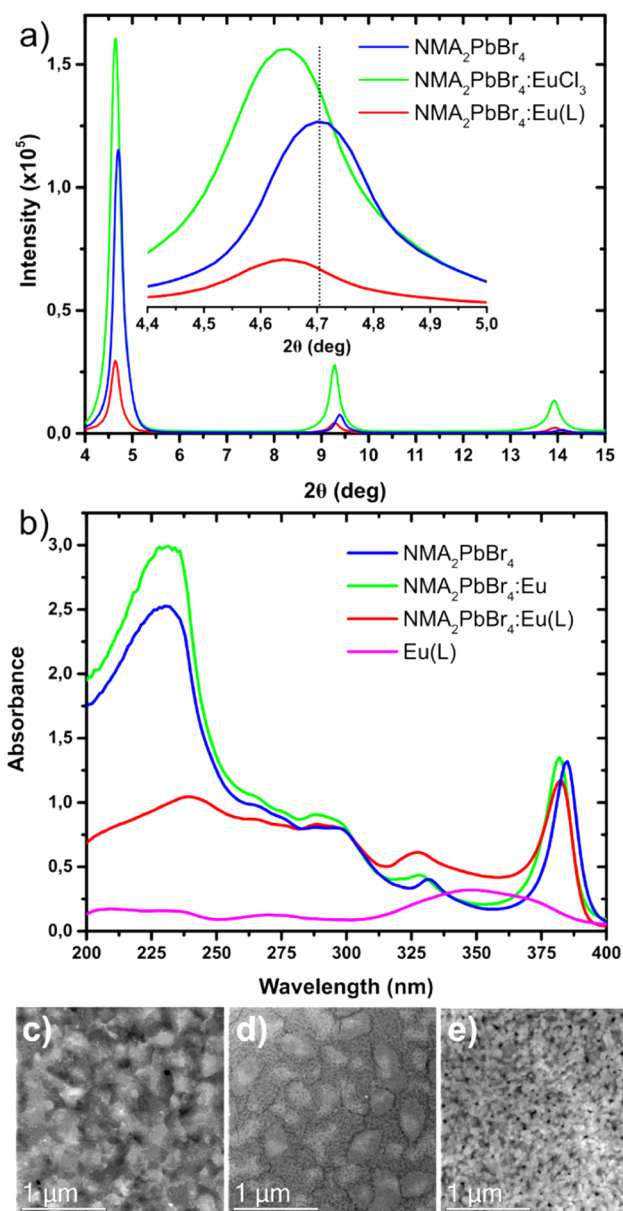


Figure 2. (a) XRD pattern and (b) absorption spectra of perovskite thin films. High-angle annular dark-field STEM (HAADF-STEM) images of (c) $\text{NMA}_2\text{PbBr}_4$, (d) $\text{NMA}_2\text{PbBr}_4:\text{Eu}$, (e) $\text{NMA}_2\text{PbBr}_4:\text{Eu(L)}$.

evident by the increase in absorbance around 350 nm in $\text{NMA}_2\text{PbBr}_4:\text{Eu(L)}$ and confirmed by Fourier-transform infrared (FTIR) spectra (Figure S3).

We further characterized the materials using transmission electron microscopy (TEM) operating in scanning TEM (STEM) mode combined with energy dispersive X-ray spectroscopy (EDS) (Figures 2c–e and S4–S8). Compared to the other two systems, $\text{NMA}_2\text{PbBr}_4:\text{Eu(L)}$ exhibits smaller grains which likely helps to release the lattice strain induced by the inclusion of the bulky complex. Eu/Pb molar ratios of around 12 and 14% were found in $\text{NMA}_2\text{PbBr}_4:\text{Eu}$ and $\text{NMA}_2\text{PbBr}_4:\text{Eu(L)}$, respectively, in good agreement with the starting stoichiometry (Figures S5 and S6). Fluorine and phosphorus were also detected in $\text{NMA}_2\text{PbBr}_4:\text{Eu(L)}$, which was indicative of the presence of the europium complex ligand and counter ion (Figure S6). In all three samples, we found non-uniformities at the sub μ -length scale which are attributed to Pb-rich regions,

likely related to the precipitation of Pb nanoparticles (Figures S7 and S8). Apart from these, both the STEM images and the elemental maps did not reveal significant phase segregations, indicating a uniform distribution of the dopant across the sample, good matrix/dopant intermixing, and absence of dopant clustering at the grain boundaries.

Figure 3 compares the steady-state PL employing 10% mol content of Eu^{3+} ; the trends for different doping concentrations are shown in Figure S9. $\text{NMA}_2\text{PbBr}_4$ is characterized by the narrowband excitonic emission at 389 nm and a secondary band peaked at 564 nm related to the NMA triplet emission.⁴⁴ After introduction of Eu^{3+} ions, the five sharp emission bands peaking at 576, 589, 611, 648, and 697 nm, characteristic of the Eu^{3+} intraconfigurational transitions $^5\text{D}_0 \rightarrow ^7\text{F}_J$ ($J = 0-4$) appear overlapped with the triplet emission. Among these, $J = 0, 2, 3, 4$ are forced ED transitions, implying that they are strictly forbidden by selection rules for purely electronic transitions when Eu^{3+} occupies a site with strict center of symmetry. On the contrary, $^5\text{D}_0 \rightarrow ^7\text{F}_1$ is a magnetic dipole transition, which is forbidden only by spin but allowed by the Laporte selection rule.³³ As such, in a strictly octahedral crystal field, only the $^5\text{D}_0 \rightarrow ^7\text{F}_1$ transition at 589 nm is expected to be observed.²⁰ Doping with Eu^{3+} proceeds with partial substitution of Pb^{2+} so that Eu^{3+} would occupy an octahedral site. The fact that all five transitions are visible in the PL spectrum is evidence that strong deviations from the inversion symmetry is reached,³³ which can be derived from concomitant contributions involving strong octahedral distortion, the spatial arrangement of the nearest neighbors (e.g., organic cations), and the symmetry group of the crystal lattice. In fact, the appearance of the weak $^5\text{D}_0 \rightarrow ^7\text{F}_0$ at 576 nm is further indication that Eu^{3+} occupies a site with either C_{nv} , C_n , or C_s symmetry.²⁰ We also explored the tuning of the host band gap by partial substitution of Br with Cl using the stoichiometry $\text{NMA}_2\text{PbCl}_x\text{Br}_{4-x}$ (Figure 3d,e). Chlorine addition causes a 20 nm blueshift of the excitonic absorption and PL, jointly with the appearance of a very broad band peaked at 500 nm characteristic of trap emission in layered perovskites;³¹ here, NMA triplet emission is observed as a shoulder at 560 nm. Despite the band gap shift, emission from Eu^{3+} is not significantly changed (Figure 3e), suggesting that the host band gap does not impact the transfer efficiency, contrary to what was previously observed with Mn^{2+} .⁸ In order to understand the possible role of the NMA triplet in the energy transfer, we synthesized europium-doped $\text{BA}_2\text{PbCl}_x\text{Br}_{4-x}$ and $\text{PEA}_2\text{PbCl}_x\text{Br}_{4-x}$ (BA = butylammonium and PEA = phenethylammonium), where the organic cation does not have an accessible triplet level. In all these systems, Eu^{3+} luminescence is not observed (Figures S10–S12), indicating that the antenna effect from NMA is crucial to sensitize the lanthanide. In fact, we do observe partial quenching of the NMA phosphorescence upon europium doping (Figures 3 and S9 and S10). However, the clear presence of residual emission from NMA indicates that the transfer is not complete, thus limiting the PLQY which remains low (about 0.3%, comparable to the undoped material). To provide a more optimized energy level alignment for the transfer to europium, as well as a rigid metal-ion environment preventing de-excitation of the excited state through coupling with lattice vibrations, we protected Eu^{3+} with tta ligands. Once the complex is formed, the $^5\text{D}_0 \rightarrow ^7\text{F}_2$ transition at 611 nm is strongly enhanced and dominates the bright red emission of $\text{NMA}_2\text{PbBr}_4:\text{Eu(L)}$ and $\text{NMA}_2\text{PbCl}_x\text{Br}_{4-x}:\text{Eu(L)}$ (Figure 3c,f). $^5\text{D}_0 \rightarrow ^7\text{F}_2$ is called the “hypersensitive transition”²⁰ as it is very sensitive to the nature of the ligands surrounding Eu^{3+} and its local geometry. The

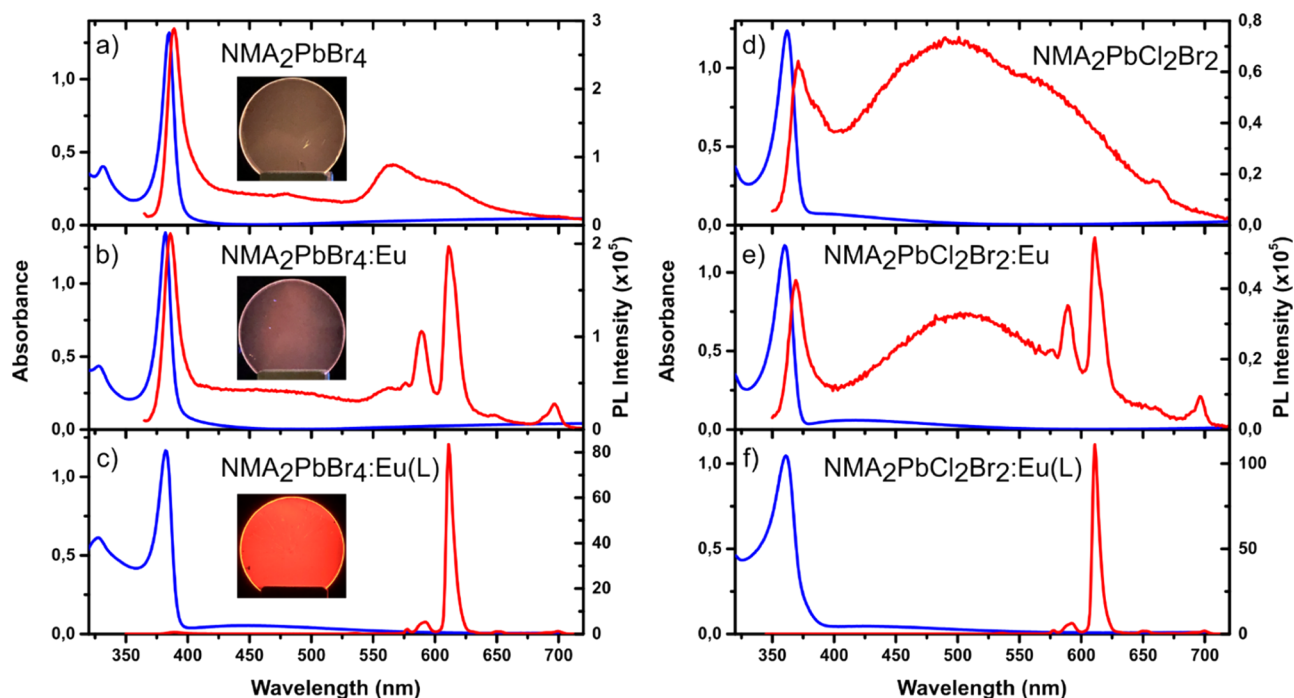


Figure 3. Absorption (blue) and PL (red) spectra of pristine and doped perovskites. For PL measurements, pump excitations of 350 and 330 nm are used for the series of $\text{NMA}_2\text{PbBr}_4$ and $\text{NMA}_2\text{PbCl}_2\text{Br}_2$ perovskites, respectively. The insets show the luminescence of perovskite films under 350 nm excitation.

intensity ratio $R = I(^5\text{D}_0 \rightarrow ^7\text{F}_2)/I(^5\text{D}_0 \rightarrow ^7\text{F}_1)$ is 1.8 and 16.2 for $\text{NMA}_2\text{PbBr}_4:\text{Eu}$ and $\text{NMA}_2\text{PbBr}_4:\text{Eu(L)}$, respectively, as a result of the strong asymmetry imparted by tta ligands and their higher polarizability compared to the halides surrounding Eu^{3+} in $\text{NMA}_2\text{PbBr}_4:\text{Eu}$. The narrower emission of $\text{NMA}_2\text{PbBr}_4:\text{Eu(L)}$ also suggests a weaker coupling with the vibrations of the host matrix. Emission from the perovskite can be exploited to excite the complex if spectral overlap between the perovskite emission and Eu(L) absorption is realized.¹⁶ This occurs only partially in $\text{NMA}_2\text{PbBr}_4$, while a better spectral overlap can be achieved by chlorine addition (Figure S13); however, the emergence of the broadband Stokes-shifted emission at high chlorine contents limits the extent to which this strategy can be used. We obtained PLQYs of 9 and 13% for $\text{NMA}_2\text{PbBr}_4:\text{Eu(L)}$ and $\text{NMA}_2\text{PbCl}_2\text{Br}_2:\text{Eu(L)}$, respectively, which represent a ~ 30 -fold enhancement compared to that of $\text{NMA}_2\text{PbBr}_4:\text{Eu}$.

The photoexcitation map of $\text{NMA}_2\text{PbBr}_4:\text{Eu}$ shows an excellent match of the perovskite absorption profile with both the NMA triplet emission and europium luminescence (Figure 4a; the photoexcitation map of the undoped $\text{NMA}_2\text{PbBr}_4$ is shown in Figure S14). This is in agreement with a process involving energy funneling from the excitons in the $[\text{PbBr}_4]^{2-}$ layers to the organic sheets and final transfer from the NMA triplet to the lanthanide. On the other hand, $\text{NMA}_2\text{PbBr}_4:\text{Eu(L)}$ shows a different photoexcitation profile (Figure 4b), with the europium emission tracing the absorption profile of the Eu(L) complex, indicating that Eu sensitization is mainly derived from the tta ligands directly chelating the metal ion.

To clarify the transfer processes involved in these systems, we performed temperature- and power-dependent PL measurements (Figure 5). At low temperatures, the NMA triplet emission in $\text{NMA}_2\text{PbBr}_4$ gains strength against the excitonic emission, which is useful to identify the emission onset (Figure 5a): we estimate the NMA triplet energy from the shortest-

wavelength phosphorescent band centered around 520 nm ($19,230 \text{ cm}^{-1}$).^{37,45–47} The best resonance acceptor level of Eu^{3+} is $^5\text{D}_1$, located about $19,000 \text{ cm}^{-1}$ (526 nm) above the $^7\text{F}_0$ ground state, from which radiationless decay to the $^5\text{D}_0$ emitting level occurs before undergoing radiative recombination.^{20,37} The main processes and feeding levels involved in the Eu^{3+} sensitization and the Eu^{3+} f–f radiative transitions are summarized in Figure 6. Although the NMA triplet (T_{NMA}) in $\text{NMA}_2\text{PbBr}_4$ has the right energetics to populate the $^5\text{D}_1$ level of europium, the very small energy gap $T_{\text{NMA}} - ^5\text{D}_1 = 230 \text{ cm}^{-1}$ makes back transfer very favorable, thus causing strong residual phosphorescence.^{37,48,49} In fact, it is experimentally demonstrated that the triplet level of the sensitizer should be located around 1500 cm^{-1} above the acceptor level to achieve efficient transfer.^{20,37} In comparison, the triplet level of tta (T_{tta}) is located at $20,300 \text{ cm}^{-1}$ (492 nm),^{19,37} and the energy gap $T_{\text{tta}} - ^5\text{D}_1 = 1300 \text{ cm}^{-1}$ is therefore more favorable for Eu^{3+} sensitization (Figure 6). Low-temperature PL of $\text{NMA}_2\text{PbBr}_4:\text{Eu}$ (Figure 5b) shows that both the NMA phosphorescence and Eu^{3+} luminescence remain strongly competing processes down to 77 K, thanks to the thermal deactivation of the nonradiative decay pathways affecting the organic cation.^{48,50} In stark contrast, the europium luminescence dominates the emission spectrum of $\text{NMA}_2\text{PbBr}_4:\text{Eu(L)}$ throughout the entire temperature range (Figure 5c), confirming the efficient sensitization imparted by the β -diketonate ligand. Previous works on lanthanide chelates have shown that the energy transfer takes place through an electron exchange mechanism, which is strongly dependent on the donor–acceptor distance.²⁰ In the more efficient $\text{NMA}_2\text{PbBr}_4:\text{Eu(L)}$, the β -diketonate ligands help to minimize the distance by directly chelating the metal ion, with a Eu–O bond length in the order of 2.4 \AA .⁴⁰ On the other hand, in $\text{NMA}_2\text{PbBr}_4:\text{Eu}$, we expect NMA to be in the second sphere of coordination of Eu^{3+} , with an estimated distance of 4.5 \AA

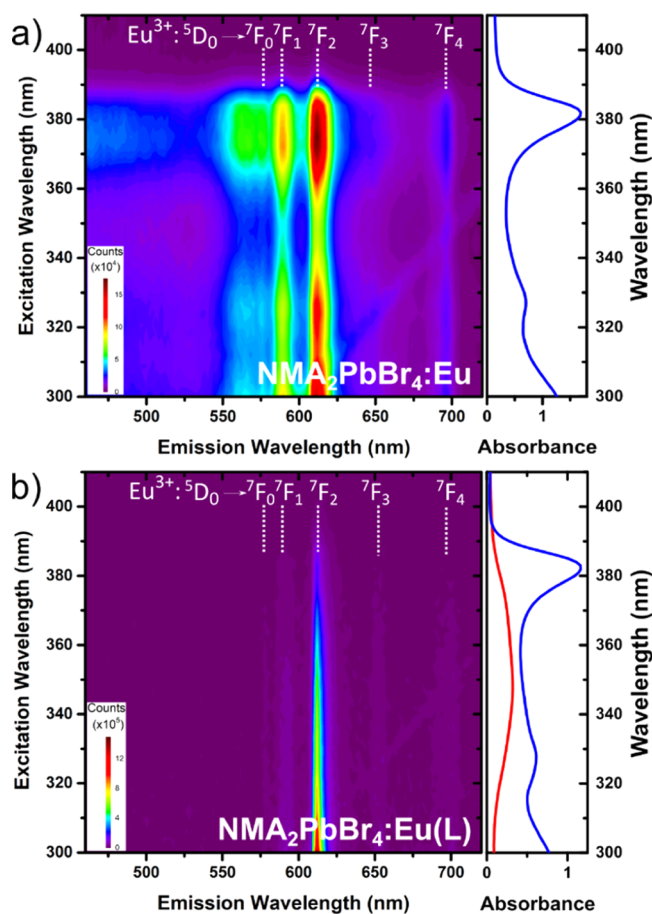


Figure 4. Photoexcitation maps of (a) NMA₂PbBr₄:Eu and (b) NMA₂PbBr₄:Eu(L). The blue lines show the absorption spectra of the corresponding perovskite, while the red line shows the absorption of the Eu(L) complex.

between Eu³⁺ and the NMA ammonium moiety,³⁹ thus representing an additional barrier to an efficient transfer. To better capture the transfer dynamics, we also performed excitation density-dependent PL measurements at 77 K (see the spectral evolution in Figure S15); the corresponding integrated spectra are shown in Figure 5d in double logarithmic scale. The excitonic emission in NMA₂PbBr₄:Eu follows the power law dependence $I = P^K$ (where I and P indicate the PL intensity and excitation power, respectively) with $K \lesssim 1$, as expected for excitonic emission with a contribution from non-radiative decay paths, such as transfer to the NMA triplet state or recombination on defects. On the other hand, the PL integrated in the range 480–900 nm (red curve in Figure 5d) clearly deviates from the linear behavior and tends to flatten at high excitation densities; the same is observed also when narrower ranges are considered, isolating the emission from either the NMA triplet or Eu³⁺ (see Figure S16). This trend suggests the saturation of NMA triplet states, which likely act as a bottleneck for the effective europium sensitization. In NMA₂PbBr₄:Eu(L), at high excitation densities, the weak excitonic emission becomes more easily visible and we also note the presence of two additional europium-based transitions (Figure S15), ⁵D₀ → ⁷F₅ (750 nm) and ⁵D₀ → ⁷F₆ (820 nm), which are rarely reported due to their weakness in molecular compounds. Here, the europium emission shows a linear power dependence similar

to that of the excitonic emission (Figure 5d), which is indicative of an efficient transfer to the lanthanide ions.

Time-resolved PL shows that both the NMA and Eu emissions are characterized by slow decay dynamics with lifetimes extending to few hundred μs, with the lanthanide being slightly longer-lived (Figure 7a). This timescale is characteristic for molecular phosphorescence and for the forbidden nature of the Eu³⁺ f–f intraconfigurational transitions. Due to the strong residual phosphorescence and the limit of our temporal resolution, we could not probe a clear NMA quenching even after europium addition. The slow decay of the NMA phosphorescence, much slower than the perovskite exciton dynamics falling in the ps range (Figure 7b), corroborates the possible saturation of NMA triplets suggested by power-dependent measurements. The excitonic emission has comparable lifetimes (around 25 ps, monoexponential fit results are presented in Supporting Information, Table S1) in both NMA₂PbBr₄ and NMA₂PbBr₄:Eu, indicating that the exciton decay dynamics are dictated by the transfer to the NMA cations and not further affected by the addition of the lanthanide. On the contrary, a more effective quenching is found in NMA₂PbBr₄:Eu(L), with the exciton lifetime decreasing to 8 ps upon addition of the complex, likely a consequence of partial energy transfer from the perovskite to the Eu(L) complex (Figure 6).

We finally note that the sharp hypersensitive ⁵D₀ → ⁷F₂ transition dominates also the electroluminescence spectrum of NMA₂PbBr₄:Eu(L), proving that the lanthanide complex embedded in the perovskite matrix can also be excited electrically (Figure S17). This highlights the possibility to exploit doping with lanthanide complexes as a strategy to improve the tunability and color purity of perovskite light-emitting devices. However, further research is necessary to improve the out-of-plane charge transport and charge injection in the wide band gap perovskites, which typically limit the efficiencies of single-layered 2D perovskite-based devices.⁸

CONCLUSIONS

Here, we have investigated doping of 2D perovskites with europium, either by direct substitutional doping with Eu³⁺ ions or by protection of Eu³⁺ in the form of the tetrakis β-diketonate complex Eu(tta)₄P(Ph)₄ Eu(L). In NMA₂PbBr₄:Eu, sensitization of the lanthanide is achieved by exploiting the antenna effect from the functional cation NMA = 1-naphthylmethylammonium. However, the non-ideal energy level alignment and binding geometry prevents the complete energy transfer to Eu³⁺ and hampers the luminescence efficiency (PLQY = 0.3%). Protection of Eu³⁺ in the form of a complex Eu(L) allows us to optimize the energetic landscape for Eu³⁺ sensitization with consequent improvement in luminescence yield, with PLQY reaching 9% in NMA₂PbBr₄:Eu(L). This work expands the range of synthetic strategies for designing functional MHPs and sets the basis for further developments. We expect that higher luminescence yields will be achieved either through the improvement of the energy transfer from the perovskite host to the europium complex by optimizing the resonance conditions of the donor/acceptor system or by adopting perovskite templating cations which can more efficiently populate the lanthanide excited state. In this regard, the formation of lanthanide-based paddle-wheel clusters linking perovskite layers represents a promising avenue.⁵¹ Furthermore, the possibility to electrically excite lanthanide complexes in the

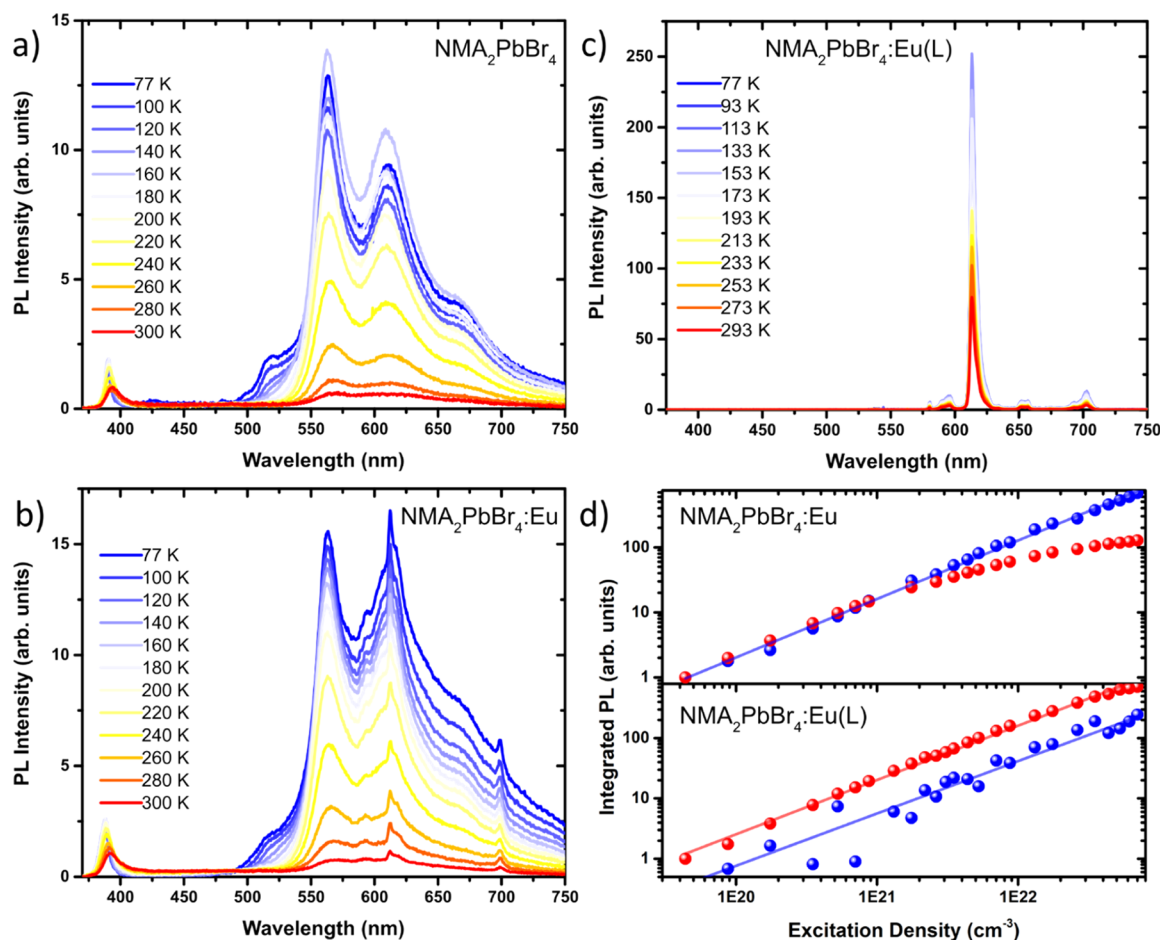


Figure 5. Temperature-dependent PL of (a) NMA₂PbBr₄, (b) NMA₂PbBr₄:Eu, and (c) NMA₂PbBr₄:Eu(L). (d) Integrated PL intensity, at 77 K, as a function of excitation density for NMA₂PbBr₄:Eu (upper panel) and NMA₂PbBr₄:Eu(L) (lower panel). The data shown in blue are related to the excitonic emission (integration in the range 380–480 nm), while the data in red color show the integration in the range 480–900 nm (see Figure S15 for the corresponding spectra). Curves in 5d have been shifted on the y-axis to allow a better comparison. Solid lines show the linear fitting to the experimental data with the power law dependence $I = P^K$; for NMA₂PbBr₄:Eu $K = 0.90 \pm 0.01$ (blue line), while for NMA₂PbBr₄:Eu(L) $K = 0.90 \pm 0.01$ (red line), and $K = 0.87 \pm 0.05$ (blue line).

perovskite matrix opens the way to their application in perovskite light-emitting devices with improved color purity.

EXPERIMENTAL SECTION

Materials. 1-Naphtylmethylamine (97%, Sigma-Aldrich), lead bromide PbBr₂ (TCI), lead chloride PbCl₂ (99.999% Sigma-Aldrich), europium(III) chloride EuCl₃ (99.99% Sigma-Aldrich), EuCl₃·6H₂O (99.9% Sigma-Aldrich), DMF (anhydrous, Sigma-Aldrich), hydrobromic acid HBr (48% in water, Sigma-Aldrich), 4,4,4-trifluoro-1-(2-thienyl)-1,3-butadione (Htta, thenoyltrifluoroacetone) (99%, Sigma-Aldrich), tetraphenylphosphonium chloride P(Ph)₄Cl (98%, Sigma-Aldrich), sodium hydroxide NaOH (Sigma-Aldrich), tetrahydrofuran THF (99.9%, Sigma-Aldrich), and dichloromethane DCM (anhydrous, Sigma-Aldrich).

Synthesis of 1-NMA Bromide (NMA)Br. 1-Naphtylmethylamine (1.5 mL, 0.01 mmol) was dissolved in 40 mL of THF, and 3.3 mL of HBr 48% (3 equivalents) was added dropwise to the solution kept in an ice bath under vigorous magnetic stirring. After 3 h, the bromide salt was precipitated by addition of dichloromethane. The powder was again dissolved in THF and precipitated with DCM, repeating the washing cycle three times. The resulting white powder of (NMA)Br was collected by filtration and dried under vacuum at 60 °C in a rotary evaporator.

Synthesis of Europium Complex Eu(tta)₄P(Ph)₄. Eu(tta)₄P(Ph)₄ was synthesized following a previously reported procedure.¹⁷ Htta (20 mmol) was deprotonated with 20 mL of a 1 M NaOH water

solution. P(Ph)₄Cl (12 mmol) was dissolved in ethanol and added to the Htta solution. EuCl₃·6H₂O (5 mmol) was dissolved in ethanol and added dropwise to the ligand's solution, causing the immediate precipitation of the complex. The resulting powder was filtered and washed three times with water and finally recrystallized from DCM (two times). The resulting light orange crystals were then recovered by filtration and dried under vacuum.

Perovskite Synthesis. NMA₂PbBr₄ was synthesized by mixing (NMA)Br and PbBr₂ in 2:1 M ratio in DMF to achieve the desired concentration (thin films for optical and XRD characterizations were obtained from 0.25 M solutions). For the doped perovskites NMA₂PbBr₄:Eu and NMA₂PbBr₄:Eu(L), EuCl₃ or Eu(tta)₄P(Ph)₄ was, respectively, added to the precursor solution, both in the amount of 10% mol with respect to the lead content unless otherwise stated. All solutions were heated for 1 h at 100 °C and then spin-coated on fused silica substrates at 5000 rpm for 30 s. The films were finally annealed on a hotplate at 100 °C for 15 min. The entire procedure was performed in a glovebox under N₂ atmosphere.

Structural and Morphological Characterization. XRD experiments were done with a BRUKER D8 ADVANCE with Bragg-Brentano geometry, Cu K α radiation ($\lambda = 1.54056 \text{ \AA}$), step increment of 0.02°, and 1 s of acquisition time. Morphological analyses and elemental mapping were carried out using an image-C_s-corrected JEM-2200FS TEM (Schottky emitter), operated at 200 kV, in HAADF-STEM imaging mode. Elemental analysis and mapping were performed with a Bruker energy-dispersive X-ray spectrometer based on a XFlash-

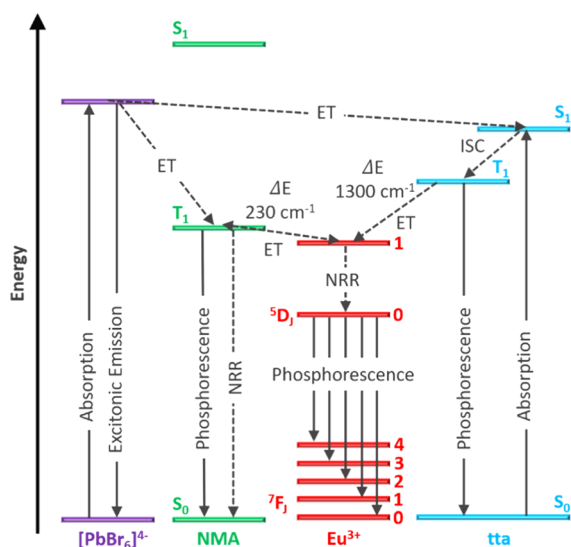


Figure 6. Schematic energy level diagram showing the main transitions occurring in the doped systems. Trapping processes and trap emission from the perovskite are not represented. The energy levels of tta are from external refs 19 and 37. S = singlet state; T = triplet state; ET = energy transfer; NRR = non-radiative relaxation; ISC = intersystem crossing.

5060 SDD. Elemental quantification was done by the Cliff–Lorimer method using the L, K, L, K series for Pb, Br, Eu, and Cl, respectively. Integration of the same peaks was used for the elemental maps. Perovskite films were spin-coated on standard TEM silicon nitride windows on a silicon frame from Norcada (NT050X) (silicon thickness = 200 μm ; nitride thickness 30 nm; window size 0.5 mm \times 0.5 mm). The sample was mounted on an analytical TEM holder, with only Be components in the electron-irradiated region, in order to minimize the background in the EDS spectra.

Spectroscopic Characterization. UV/VIS/NIR spectrophotometer λ 1050, PerkinElmer equipped with integrating sphere (module 150 mm InGaAs Int. Sphere) was used for absorption measurements. NanoLog (HORIBA Jobin Yvon) was used for steady-state PL measurements; absolute PLQY was measured using an integrating sphere (Quanta- ϕ) in combination with the NanoLog spectrofluorometer and using an excitation wavelength of 330 nm. Temperature- and pump fluence-dependent measurements were performed under nitrogen atmosphere using a Linkam Stage cooled with liquid nitrogen, exciting the sample with the third harmonic (355 nm) from a Nd:YAG Picolo-AOT laser (pulse length of approximately 1000 ps, 1 kHz repetition rate) focused on the sample with a 10 cm lens. PL was detected using a Maya1000 visible spectrometer. FTIR spectra were measured with a Bruker VERTEX 70 spectrometer in attenuated total reflectance mode with a Ge crystal. Measurements comprised 32 scans with 1 cm^{-1} resolution. For the analysis, perovskite films were deposited on silicon substrates by spin-coating precursor solutions with a concentration of 1 M in DMF. TRPL measurements on μs timescales were performed using an Andor iStar 320T ICCD-gated camera coupled to a Shamrock 303i spectrograph using a temporal step size of 100 μs and a spectral resolution of 0.2 nm. All measurements were performed in vacuum. As a pump, the third harmonic (355 nm) from a Nd:YAG Picolo-AOT laser was used, with a pulse length of 900 ps, repetition rate of 300 Hz, and pulse energy of 48 $\mu\text{J}/\text{cm}^2$. TRPL of the excitonic feature in the ps range was performed using a Hamamatsu streak camera and a Coherent Chameleon oscillator (pulse duration 30 fs, repetition rate 80 MHz) as a pump, using a pump wavelength λ = 380 nm, and a fluence I_{pump} = 790 mW/cm^2 , corresponding to a pulse energy of 9.87 nJ/cm^2 . The measurements on $\text{NMA}_2\text{PbBr}_4$ and $\text{NMA}_2\text{PbBr}_4:\text{Eu}$ were performed using a measurement window 800 ps long, corresponding to a resolution of 8 ps as computed from the instrument response function (IRF). Measurements on

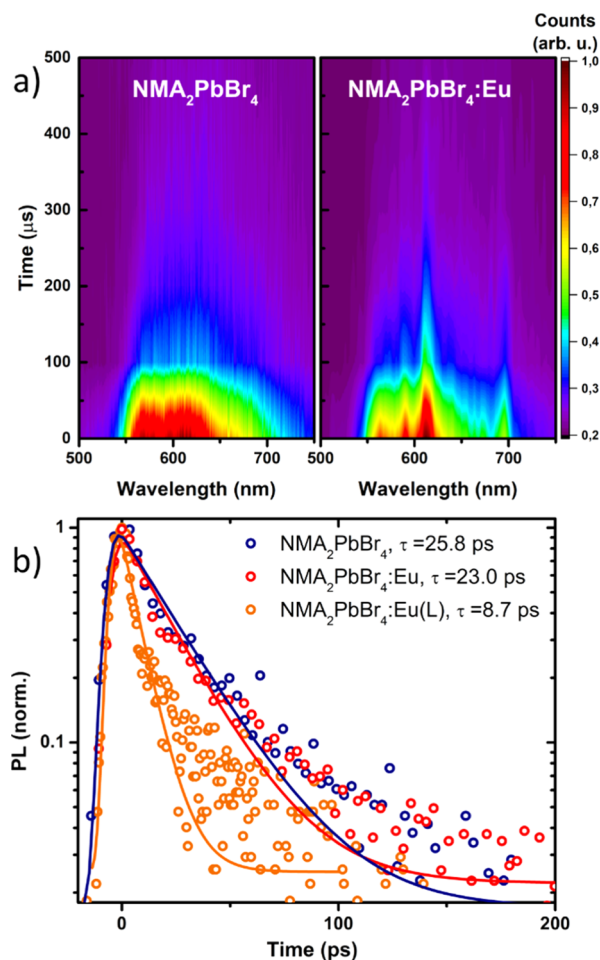


Figure 7. (a) Time-resolved PL maps of the NMA phosphorescence and europium luminescence in $\text{NMA}_2\text{PbBr}_4$ (left panel) and $\text{NMA}_2\text{PbBr}_4:\text{Eu}$ (right panel). (b) Comparison of the exciton decay dynamics in the range 380–395 nm for the doped and undoped $\text{NMA}_2\text{PbBr}_4$ perovskite. The solid lines show the result of a monoexponential decay fit.

$\text{NMA}_2\text{PbBr}_4:\text{Eu(L)}$ were conducted using a 240 ps window, with a corresponding resolution of 2.8 ps. The excitonic emission lifetime was calculated by integrating the decay in the exciton spectral region (380–395 nm) and then fitting the normalized decay with a monoexponential gaussian decay $I(t) = I_0 e^{-(t-t_0)/\tau}$ convoluted with the IRF; the fit parameters are reported in Table S1.

■ ASSOCIATED CONTENT

Supporting Information

The Supporting Information is available free of charge at <https://pubs.acs.org/doi/10.1021/acs.chemmater.0c04097>.

LED fabrication method, XRD data, optical characterization, STEM elemental maps, and electroluminescence measurements (PDF)

■ AUTHOR INFORMATION

Corresponding Authors

Daniele Cortecchia – Centre for Nano Science and Technology (CNST@PoliMi), Istituto Italiano di Tecnologia, Milan 20133, Italy; orcid.org/0000-0001-8623-9191; Email: Daniele.Cortecchia@iit.it

Annamaria Petrozza – Centre for Nano Science and Technology (CNST@PoliMi), Istituto Italiano di Tecnologia, Milan

20133, Italy; orcid.org/0000-0001-6914-4537;
Email: Annamaria.Petrozza@iit.it

Authors

Wojciech Mróz – Centre for Nano Science and Technology (CNST@PoliMi), Istituto Italiano di Tecnologia, Milan 20133, Italy; orcid.org/0000-0002-4534-6238

Giulia Folpini – Centre for Nano Science and Technology (CNST@PoliMi), Istituto Italiano di Tecnologia, Milan 20133, Italy

Tetiana Borzda – Centre for Nano Science and Technology (CNST@PoliMi), Istituto Italiano di Tecnologia, Milan 20133, Italy

Luca Leoncino – Electron Microscopy Facility, Istituto Italiano di Tecnologia, Genova 16163, Italy

Ada Lili Alvarado-Leaños – Centre for Nano Science and Technology (CNST@PoliMi), Istituto Italiano di Tecnologia, Milan 20133, Italy

Emily Mae Speller – Centre for Nano Science and Technology (CNST@PoliMi), Istituto Italiano di Tecnologia, Milan 20133, Italy

Complete contact information is available at:
<https://pubs.acs.org/10.1021/acs.chemmater.0c04097>

Author Contributions

D.C. conceived the idea for the manuscript and designed the experiments. D.C. synthesized and characterized the materials. W.M. fabricated and characterized LEDs and contributed to planning the experiments. G.F., T.B., and A.L.A.L. performed time-resolved and power- and temperature-dependent measurements. L.L. performed STEM-EDS measurements. EMS acquired FTIR spectra. A.P. supervised and coordinated the work. The manuscript was written through contributions of all authors. All authors have given approval to the final version of the manuscript.

Notes

The authors declare no competing financial interest.

ACKNOWLEDGMENTS

This project has received funding from the European Union's Horizon 2020 research and innovation programme under the Marie Skłodowska-Curie grant agreement no. 839480 (PERICLEs). The authors acknowledge funding from the European Union's Horizon 2020 MSCA Innovative Training Network under grant agreement no. 764787 and from the ERC project SOPHY under grant agreement no. 771528. The authors thank Rosaria Brescia for the assistance for STEM characterization and Alex J. Barker for technical support.

ABBREVIATIONS

NMA, 1-naphthylmethylamine; tta, thenoyltrifluoroacetate; Ph, phenyl; BA, butylammonium; PEA, phenethylammonium; HAADF, high-angle annular dark field; STEM, scanning transmission electron microscope

REFERENCES

- (1) Chin, X. Y.; Cortecchia, D.; Yin, J.; Bruno, A.; Soci, C. Lead iodide perovskite light-emitting field-effect transistor. *Nat. Commun.* **2015**, *6*, 7383.
- (2) Xu, W.; Hu, Q.; Bai, S.; Bao, C.; Miao, Y.; Yuan, Z.; Borzda, T.; Barker, A. J.; Tyukalova, E.; Hu, Z.; Kaweck, M.; Wang, H.; Yan, Z.; Liu, X.; Shi, X.; Uvdal, K.; Fahlman, M.; Zhang, W.; Duchamp, M.; Liu, J.-M.; Petrozza, A.; Wang, J.; Liu, L.-M.; Huang, W.; Gao, F. Rational

molecular passivation for high-performance perovskite light-emitting diodes. *Nat. Photonics* **2019**, *13*, 418–424.

(3) Gandini, M.; Villa, I.; Beretta, M.; Gotti, C.; Imran, M.; Carulli, F.; Fantuzzi, E.; Sassi, M.; Zaffalon, M.; Brofferio, C.; Manna, L.; Beverina, L.; Vedda, A.; Fasoli, M.; Gironi, L.; Brovelli, S. Efficient, fast and reabsorption-free perovskite nanocrystal-based sensitized plastic scintillators. *Nat. Nanotechnol.* **2020**, *15*, 462–468.

(4) Jia, Y.; Kerner, R. A.; Grede, A. J.; Rand, B. P.; Giebink, N. C. Continuous-wave lasing in an organic–inorganic lead halide perovskite semiconductor. *Nat. Photonics* **2017**, *11*, 784–788.

(5) Lu, C.-H.; Biesold-McGee, G. V.; Liu, Y.; Kang, Z.; Lin, Z. Doping and ion substitution in colloidal metal halide perovskite nanocrystals. *Chem. Soc. Rev.* **2020**, *49*, 4953–5007.

(6) Xu, L.; Yuan, S.; Zeng, H.; Song, J. A comprehensive review of doping in perovskite nanocrystals/quantum dots: evolution of structure, electronics, optics, and light-emitting diodes. *Mater. Today Nano* **2019**, *6*, 100036.

(7) Guria, A. K.; Dutta, S. K.; Adhikari, S. D.; Pradhan, N. Doping Mn²⁺ in Lead Halide Perovskite Nanocrystals: Successes and Challenges. *ACS Energy Lett.* **2017**, *2*, 1014–1021.

(8) Cortecchia, D.; Mróz, W.; Neutzner, S.; Borzda, T.; Folpini, G.; Brescia, R.; Petrozza, A. Defect Engineering in 2D Perovskite by Mn(II) Doping for Light-Emitting Applications. *Chem.* **2019**, *5*, 2146–2158.

(9) Sheikh, T.; Nag, A. Mn Doping in Centimeter-Sized Layered 2D Butylammonium Lead Bromide (BA₂PbBr₄) Single Crystals and Their Optical Properties. *J. Phys. Chem. C* **2019**, *123*, 9420–9427.

(10) Parobek, D.; Roman, B. J.; Dong, Y.; Jin, H.; Lee, E.; Sheldon, M.; Son, D. H. Exciton-to-Dopant Energy Transfer in Mn-Doped Cesium Lead Halide Perovskite Nanocrystals. *Nano Lett.* **2016**, *16*, 7376–7380.

(11) Meinardi, F.; Akkerman, Q. A.; Bruni, F.; Park, S.; Mauri, M.; Dang, Z.; Manna, L.; Brovelli, S. Doped Halide Perovskite Nanocrystals for Reabsorption-Free Luminescent Solar Concentrators. *ACS Energy Lett.* **2017**, *2*, 2368–2377.

(12) Kroupa, D. M.; Roh, J. Y.; Milstein, T. J.; Creutz, S. E.; Gamelin, D. R. Quantum-Cutting Ytterbium-Doped CsPb(Cl_{1-x}Br_x)₃ Perovskite Thin Films with Photoluminescence Quantum Yields over 190%. *ACS Energy Lett.* **2018**, *3*, 2390–2395.

(13) Milstein, T. J.; Kroupa, D. M.; Gamelin, D. R. Picosecond Quantum Cutting Generates Photoluminescence Quantum Yields Over 100% in Ytterbium-Doped CsPbCl₃ Nanocrystals. *Nano Lett.* **2018**, *18*, 3792–3799.

(14) Pan, G.; Bai, X.; Yang, D.; Chen, X.; Jing, P.; Qu, S.; Zhang, L.; Zhou, D.; Zhu, J.; Xu, W.; Dong, B.; Song, H. Doping Lanthanide into Perovskite Nanocrystals: Highly Improved and Expanded Optical Properties. *Nano Lett.* **2017**, *17*, 8005–8011.

(15) Zhou, D.; Liu, D.; Pan, G.; Chen, X.; Li, D.; Xu, W.; Bai, X.; Song, H. Cerium and Ytterbium Codoped Halide Perovskite Quantum Dots: A Novel and Efficient Downconverter for Improving the Performance of Silicon Solar Cells. *Adv. Mater.* **2017**, *29*, 1704149.

(16) McGehee, M. D.; Bergstedt, T.; Zhang, C.; Saab, A. P.; O'Regan, M. B.; Bazan, G. C.; Srdanov, V. I.; Heeger, A. J. Narrow Bandwidth Luminescence from Blends with Energy Transfer from Semiconducting Conjugated Polymers to Europium Complexes. *Adv. Mater.* **1999**, *11*, 1349–1354.

(17) Mezyk, J.; Mróz, W.; Mech, A.; Giovannella, U.; Meinardi, F.; Botta, C.; Vercelli, B.; Tubino, R. Diffusion-mediated resonant energy transfer in lanthanide-based polymer white-light-emitting diodes. *Phys. Chem. Chem. Phys.* **2009**, *11*, 10152–10156.

(18) Nakamura, K.; Hasegawa, Y.; Kawai, H.; Yasuda, N.; Kanehisa, N.; Kai, Y.; Nagamura, T.; Yanagida, S.; Wada, Y. Enhanced Lasing Properties of Dissymmetric Eu(III) Complex with Bidentate Phosphine Ligands. *J. Phys. Chem. A* **2007**, *111*, 3029–3037.

(19) Shahi, P. K.; Singh, A. K.; Singh, S. K.; Rai, S. B.; Ullrich, B. Revelation of the Technological Versatility of the Eu(TTA)₃Phen Complex by Demonstrating Energy Harvesting, Ultraviolet Light Detection, Temperature Sensing, and Laser Applications. *ACS Appl. Mater. Interfaces* **2015**, *7*, 18231–18239.

(20) Binnemans, K. Interpretation of europium(III) spectra. *Coord. Chem. Rev.* **2015**, *295*, 1–45.

- (21) Bünzli, J.-C. G.; Piguet, C. Taking advantage of luminescent lanthanide ions. *Chem. Soc. Rev.* **2005**, *34*, 1048–1077.
- (22) Eliseeva, S. V.; Bünzli, J.-C. G. Lanthanide luminescence for functional materials and bio-sciences. *Chem. Soc. Rev.* **2010**, *39*, 189–227.
- (23) Binnemans, K. Lanthanide-Based Luminescent Hybrid Materials. *Chem. Rev.* **2009**, *109*, 4283–4374.
- (24) Wang, L.; Zhou, H.; Hu, J.; Huang, B.; Sun, M.; Dong, B.; Zheng, G.; Huang, Y.; Chen, Y.; Li, L.; Xu, Z.; Li, N.; Liu, Z.; Chen, Q.; Sun, L.-D.; Yan, C.-H. A Eu^{3+} - Eu^{2+} ion redox shuttle imparts operational durability to Pb-I perovskite solar cells. *Science* **2019**, *363*, 265–270.
- (25) Xiang, W.; Wang, Z.; Kubicki, D. J.; Tress, W.; Luo, J.; Prochowicz, D.; Akin, S.; Emsley, L.; Zhou, J.; Dietler, G.; Grätzel, M.; Hagfeldt, A. Europium-Doped CsPbI₂Br for Stable and Highly Efficient Inorganic Perovskite Solar Cells. *Joule* **2019**, *3*, 205–214.
- (26) Cheng, Y.; Shen, C.; Shen, L.; Xiang, W.; Liang, X. Tb³⁺, Eu³⁺ Co-doped CsPbBr₃ QDs Glass with Highly Stable and Luminous Adjustable for White LEDs. *ACS Appl. Mater. Interfaces* **2018**, *10*, 21434–21444.
- (27) Li, Q.; Liu, Y.; Chen, P.; Hou, J.; Sun, Y.; Zhao, G.; Zhang, N.; Zou, J.; Xu, J.; Fang, Y.; Dai, N. Excitonic Luminescence Engineering in Tervalent-Europium-Doped Cesium Lead Halide Perovskite Nanocrystals and Their Temperature-Dependent Energy Transfer Emission Properties. *J. Phys. Chem. C* **2018**, *122*, 29044–29050.
- (28) Pan, G.; Bai, X.; Xu, W.; Chen, X.; Zhou, D.; Zhu, J.; Shao, H.; Zhai, Y.; Dong, B.; Xu, L.; Song, H. Impurity Ions Codoped Cesium Lead Halide Perovskite Nanocrystals with Bright White Light Emission toward Ultraviolet–White Light-Emitting Diode. *ACS Appl. Mater. Interfaces* **2018**, *10*, 39040–39048.
- (29) Wang, Y.; Zhu, Y.; Yang, G.; Yang, X.; Xu, X.; Huang, J.; Cui, S. Highly efficient silica-coated Eu^{3+} and Mn^{2+} doped CsPbCl₃ perovskite quantum dots for application in light-emitting diodes. *Appl. Phys. Express* **2019**, *12*, 072006.
- (30) Wu, J.; Bai, H.; Qu, W.; Cao, G.; Zhang, Y.; Yu, J. Preparation of Eu^{3+} -doped CsPbBr₃ quantum-dot microcrystals and their luminescence properties. *Opt. Mater.* **2019**, *97*, 109454.
- (31) Cortecchia, D.; Yin, J.; Petrozza, A.; Soci, C. White light emission in low-dimensional perovskites. *J. Mater. Chem. C* **2019**, *7*, 4956–4969.
- (32) Hasegawa, Y.; Kitagawa, Y.; Nakanishi, T. Effective photosensitized, electrosensitized, and mechanosensitized luminescence of lanthanide complexes. *NPG Asia Mater.* **2018**, *10*, 52–70.
- (33) Blasse, G.; Brill, A.; Nieuwpoort, W. C. On the Eu^{3+} fluorescence in mixed metal oxides: Part I—The crystal structure sensitivity of the intensity ratio of electric and magnetic dipole emission. *J. Phys. Chem. Solids* **1966**, *27*, 1587–1592.
- (34) Silva, A. I. S.; Lima, N. B. D.; Simas, A. M.; Gonçalves, S. M. C. Europium Complexes: Luminescence Boost by a Single Efficient Antenna Ligand. *ACS Omega* **2017**, *2*, 6786–6794.
- (35) Leonard, J. P.; Jensen, P.; McCabe, T.; O'Brien, J. E.; Peacock, R. D.; Kruger, P. E.; Gunnlaugsson, T. Self-Assembly of Chiral Luminescent Lanthanide Coordination Bundles. *J. Am. Chem. Soc.* **2007**, *129*, 10986–10987.
- (36) Plush, S. E.; Clear, N. A.; Leonard, J. P.; Fanning, A.-M.; Gunnlaugsson, T. The effect on the lanthanide luminescence of structurally simple Eu(III) cyclen complexes upon deprotonation of metal bound water molecules and amide based pendant arms. *Dalton Trans.* **2010**, *39*, 3644–3652.
- (37) Susumu, S.; Masanobu, W. Relations between Intramolecular Energy Transfer Efficiencies and Triplet State Energies in Rare Earth β -diketone Chelates. *Bull. Chem. Soc. Jpn.* **1970**, *43*, 1955–1962.
- (38) Jemli, K.; Audebert, P.; Galmiche, L.; Trippé-Allard, G.; Garrot, D.; Lauret, J.-S.; Deleporte, E. Two-Dimensional Perovskite Activation with an Organic Luminophore. *ACS Appl. Mater. Interfaces* **2015**, *7*, 21763–21769.
- (39) Du, K.-z.; Tu, Q.; Zhang, X.; Han, Q.; Liu, J.; Zauscher, S.; Mitzi, D. B. Two-Dimensional Lead(II) Halide-Based Hybrid Perovskites Templated by Acene Alkylamines: Crystal Structures, Optical Properties, and Piezoelectricity. *Inorg. Chem.* **2017**, *56*, 9291–9302.
- (40) Knall, A. C.; Tscherner, M.; Noormofidi, N.; Pein, A.; Saf, R.; Mereiter, K.; Ribitsch, V.; Stelzer, F.; Slugovc, C. Nonradiative deactivation of europium(III) luminescence as a detection scheme for moisture. *Analyst* **2012**, *137*, 563–566.
- (41) Melendez, F. J.; Castro, M. E.; Portillo-Moreno, O.; Hernández-Téllez, G.; Moreno-Morales, G. E.; Gutiérrez-Argüelles, D.; Palomino-Merino, R.; Rubio-Rosas, E.; Gutiérrez-Pérez, R. Experimental and DFT Study of the Photoluminescent Green Emission Band of Halogenated (-F, -Cl, and -Br) Imines. *Molecules* **2019**, *24*, 3304.
- (42) Guerrini, M.; Cocchi, C.; Calzolari, A.; Varsano, D.; Corni, S. Interplay between Intra- and Intermolecular Charge Transfer in the Optical Excitations of J-Aggregates. *J. Phys. Chem. C* **2019**, *123*, 6831–6838.
- (43) Li, F.; Gao, N.; Xu, H.; Liu, W.; Shang, H.; Yang, W.; Zhang, M. Relationship between Molecular Stacking and Optical Properties of 9,10-Bis((4-N,N-dialkylamino)styryl) Anthracene Crystals: The Co-operation of Excitonic and Dipolar Coupling. *Chem.—Eur. J.* **2014**, *20*, 9991–9997.
- (44) Ema, K.; Inomata, M.; Kato, Y.; Kunugita, H.; Era, M. Nearly Perfect Triplet-Triplet Energy Transfer from Wannier Excitons to Naphthalene in Organic-Inorganic Hybrid Quantum-Well Materials. *Phys. Rev. Lett.* **2008**, *100*, 257401.
- (45) Bortoluzzi, M.; Gobbo, A.; Palù, A.; Enrichi, F.; Vomiero, A. Luminescent lanthanide complexes with phosphoramidate and arylphosphonic diamide ligands. *Chem. Pap.* **2020**, *74*, 3693–3704.
- (46) Rao, X.; Song, T.; Gao, J.; Cui, Y.; Yang, Y.; Wu, C.; Chen, B.; Qian, G. A Highly Sensitive Mixed Lanthanide Metal–Organic Framework Self-Calibrated Luminescent Thermometer. *J. Am. Chem. Soc.* **2013**, *135*, 15559–15564.
- (47) Xu, C. Photophysical properties of lanthanide complexes with 5-nitro-1,10-phenanthroline. *Monatsh. Chem.* **2010**, *141*, 631–635.
- (48) Li, L.; Zhu, Y.; Zhou, X.; Brites, C. D. S.; Ananias, D.; Lin, Z.; Paz, F. A. A.; Rocha, J.; Huang, W.; Carlos, L. D. Visible-Light Excited Luminescent Thermometer Based on Single Lanthanide Organic Frameworks. *Adv. Funct. Mater.* **2016**, *26*, 8677–8684.
- (49) Rocha, J.; Brites, C. D. S.; Carlos, L. D. Lanthanide Organic Framework Luminescent Thermometers. *Chem.—Eur. J.* **2016**, *22*, 14782–14795.
- (50) Andriotou, D.; Diamantis, S. A.; Zacharia, A.; Itskos, G.; Panagiotou, N.; Tasiopoulos, A. J.; Lazarides, T. Dual Emission in a Ligand and Metal Co-Doped Lanthanide–Organic Framework: Color Tuning and Temperature Dependent Luminescence. *Molecules* **2020**, *25*, 523.
- (51) Mercier, N.; Riou, A. An organic–inorganic hybrid perovskite containing copper paddle-wheel clusters linking perovskite layers: $[\text{Cu}(\text{O}_2\text{C}-(\text{CH}_2)_3-\text{NH}_3)_2]\text{PbBr}_4$. *Chem. Commun.* **2004**, 844–845.